

# Pore-scale study of rarefied gas flows using low-variance deviational simulation Monte Carlo method

Ferdin Don Bosco · Yonghao Zhang

Received: date / Accepted: date

**Abstract** Gaseous flow through ultra-tight porous media, e.g. shale and some high-performance insulation materials, is often rarefied, invalidating an analysis by the continuum flow theory. Such rarefied flows can be accurately described by the kinetic theory of gases which utilizes the Boltzmann equation and its simplified kinetic models. While discrete velocity methods (DVM) have been successful in directly solving these equations, the immense potential of a particle-based solution of the variance-reduced Boltzmann-BGK (Bhatnagar-Gross-Krook) equation for rarefied flows in porous media has not been exploited yet. Here, a parallel solver based on the low variance deviational simulation Monte Carlo (LVDSMC) method is developed for 3D flows, which enables pore-scale simulations using digital images of porous media samples. The unique advantage of this particle-based formulation is in providing additional insights regarding the multi-scale nature of the flow and surface/gas interactions via two new parameters, i.e. pore and surface activity respectively. Together, these two parameters can identify key flow properties of the porous media. The computational efficiency and accuracy of the current method has also been analysed, suggesting that this new solver is a powerful simulation tool to quantify flow properties of ultra-tight porous media.

**Keywords** rarefied flow · Knudsen diffusion · low-variance deviational simulation Monte Carlo method · porous media · pore-scale simulation

## 1 Introduction

The burgeoning industries with a vested interest in gas flows through ultra-tight porous media have led to the recent surge of research interests in such flows, which are prevalent in micro/nano-electronic cooling [1], nano-porous insulations [2], fuel cell technology [3], medical and biomedical devices [4], oil and gas production [5], and ablative process [6, 7] such as those in aerospace industry.

---

Ferdin Don Bosco  
Department of Mechanical and Aerospace Engineering, University of Strathclyde, Glasgow, G1 1XJ, UK  
ORCID: <https://orcid.org/0000-0002-5507-5304>; E-mail: [ferdinsagai7@gmail.com](mailto:ferdinsagai7@gmail.com)

Yonghao Zhang  
School of Engineering, The University of Edinburgh, Edinburgh, EH9 3FB, UK  
ORCID: <https://orcid.org/0000-0002-0683-7050>; E-mail: [yonghao.zhang@ed.ac.uk](mailto:yonghao.zhang@ed.ac.uk)

Due to the small dimensions of the pore space, gas flows through ultra-tight porous media are usually low-speed, highly rarefied, and extremely confined, resulting in very unique gas flow physics. When the Mach number is negligible, i.e.  $Ma \ll 1$ , any stochastic particle-based simulation method will suffer from the low signal to noise ratio, i.e. the flow velocity (signal) created by a driving mechanism is much smaller than the thermal velocity (noise) of the molecules. The gas rarefaction in the pore space is highly non-uniform, featuring co-existing regions of differing rarefactions, from continuum to free molecular flows. Such flows are characterised by significant variation in the local Knudsen number and demand a multi-scale simulation for improved understanding. In addition, these flows are highly-confined so the surface plays a major role in gas transport. Therefore, understanding of rarefied gas flow in highly confined pore spaces remains a research challenge.

The fundamental Boltzmann equation, and its simplified model equations, e.g. Bhatnagar-Gross-Krook (BGK) [8], Shakov-BGK [9] and Ellipsoidal Statistical-BGK [10] models, offer a kinetic description of the gas flow. Deterministic approaches such as lattice Boltzmann method (LBM) [11–14] and other discrete velocity methods (DVM) [15–18] are popular for pore-scale simulations. While it is established that the prevalent simulation method, namely direct simulation Monte Carlo (DSMC) is robust and handles complex boundaries with ease, it suffers from the computationally expensive sampling process to mitigate the statistical noise in the low-signal flows. The advantages of DSMC have inspired the extension/development of particle methods for such flow simulations [19–24].

A reduction of the statistical noise in the calculation of macroscopic variables can be achieved either by an increase in the number of samples or a decrease in variance in the Monte Carlo evaluation of these variables. The former method leads to an increase in the computational cost whereas, the latter results in the variance reduction techniques which reduce the computational cost dramatically. **One such approach is the direct simulation BGK (DSBGK) method [25–28], and its capability in pore-scale simulation of shale gas flows has been demonstrated [29, 30].** Recently, the variance reduction techniques were introduced for an efficient calculation of the collision integral [31–38]. In the particle-based approach, the particles are drawn from the deviation from an equilibrium state and are represented by a system of positive and negative particles, and the flow system evolves via advection and collisions of these particles. As the gas relaxes to equilibrium through collisions, decrease in the deviational particles is aligned with the relaxation time approximation. Therefore, the natural extension of the method to the BGK collision model was put forth, first using the acceptance-rejection sampling [35] and then by the ratio-of-uniforms method [36]. The latter work also demonstrated a second-order convergence in time by using a symmetrised version of the algorithm [36]. One of the key issues with the method was the conservation of mass, momentum, and energy which are only done on average (owing to the source-sink interpretation of the collision term), unlike the DSMC where conservation is ensured for every collision event. This was addressed [36] through the inclusion of mass conservation routines which monitor and minimize the residual by regenerating particles with the appropriate sign at each step. Other variants, such as modifying the importance weights of the particles [38] and improvements such as the replacement of the BGK collision operator by the McCormack kinetic model thereby enabling the simulation of a binary gas system [39] were also investigated.

Although the method was successfully deployed to study some simple problems [40–44], the application of this method has been very limited and its greater potential remains largely unexplored. In the present research, we apply this method to develop a new pore-scale simulation tool to study multi-scale flows through complex porous media.

## 2 LVDSMC and flow in porous media

### 2.1 LVDSMC method

The Boltzmann equation is the cornerstone of gas kinetic theory, which describes evolution of the single particle distribution function,  $f = f(\mathbf{r}, \mathbf{c}, t)$ , in the phase space  $(\mathbf{r}, \mathbf{c})$ , where  $\mathbf{r}$  is the spatial co-ordinate and  $\mathbf{c}$  is the molecular velocity. In porous media, the pressure gradient, which drives the flow, may be represented by a body force. Additionally, the collision process can be interpreted as relaxation of a small perturbation of  $f$  over a time  $\tau_r$ , known as the relaxation time. Under these assumptions, the governing equation of the system is given by,

$$\frac{\partial f}{\partial t} + \mathbf{c} \cdot \frac{\partial f}{\partial \mathbf{r}} + \left[ \frac{\partial f}{\partial t} \right]_{BF} = \left( \frac{\partial f}{\partial t} \right)_{coll} = \frac{f^{loc} - f}{\tau_r}, \quad (1)$$

where,

$$f^{loc} = n^{loc} (\sqrt{\pi} v_{mp}^{loc})^{-3} \exp \left[ -\frac{\|\mathbf{c} - \mathbf{u}^{loc}\|^2}{v_{mp}^{loc2}} \right], \quad (2)$$

$$\left[ \frac{\partial f}{\partial t} \right]_{BF} = c_{r_i} \left[ \zeta_P + \left( \frac{5}{2} - \frac{\|\mathbf{c} - \mathbf{u}_0\|^2}{v_{mp,0}^2} \right) \zeta_T \right] f_0, \quad (3)$$

$t$  is the time and  $f^{loc}$  is the instantaneous local distribution with  $n^{loc}$ ,  $\mathbf{u}^{loc}$ ,  $T^{loc}$  being the number density, bulk velocity, temperature respectively.  $v_{mp}^{loc} = \sqrt{\frac{2K_b T^{loc}}{m}}$  is the most probable speed with  $K_b (1.38064852 \times 10^{-23} \text{ kgm}^2/\text{Ks}^2)$  and  $m$  representing the Boltzmann constant and molecular mass respectively. Furthermore, the equation for the body force (BF) is obtained from the work of Cercignani and Daneri [45]. In the Eq. 3,  $r_i$  is the spatial co-ordinate,  $c_{r_i}$  is the molecular velocity in the direction of the body force,  $\zeta_P = \frac{L_0}{P_0} \frac{dP}{dr_i}$  and  $\zeta_T = \frac{L_0}{T_0} \frac{dT}{dr_i}$  are the non-dimensional pressure gradient and temperature gradient in the direction  $r_i$  respectively.

Expressing the distribution function as a combination of an equilibrium state and a deviation ( $f_d$ ) (see Eq. (4) below) is the key idea in the low-variance deviational simulation Monte Carlo method. The solution strategy consists of an analytical handling of the equilibrium, i.e. the Maxwell-Boltzmann distribution, see Eq. (5), while the deviation,  $f_d$ , which is not analytically treatable is integrated by a system of positive and negative particles drawn as given below:

$$f = f_{eq} + f_d, \quad (4)$$

$$f_{eq} = f_0 = f^{mb} = \frac{\rho^{mb}}{v_{mp}^{mb3} \pi^{\frac{3}{2}}} \exp \left( -\frac{\|\mathbf{c} - \mathbf{u}^{mb}\|^2}{v_{mp}^{mb2}} \right), \quad (5)$$

$$f_d(\mathbf{c}) = mW_{eff} \sum_{i=1}^N s_i \delta^3(\mathbf{x} - \mathbf{x}_i) \delta^3(\mathbf{c} - \mathbf{c}_i). \quad (6)$$

Here,  $n^{mb} (= n_0)$ ,  $\mathbf{u}^{mb} (= \mathbf{u}_0)$ , and  $v_{mp}^{mb} (= v_{mp,0}) = \sqrt{\frac{2K_b T^{mb}}{m}}$  are the number density, bulk velocity, and most probable speed at the global equilibrium,  $f_0$ . Also,  $s_i$  indicates sign of the particle, which is either +1 or -1,  $W_{eff}$  represents the number of physical particles per a simulated particle in addition to the unit deviation represented by the particle. A positive deviation particle indicates that the  $f$  is greater than  $f_{eq}$  in that phase space element and vice

versa. This stipulates that an equal number of positive and negative particles occupying the same phase space element results in no net change to the distribution function.

The method emulates the DSMC's idea of operator splitting which is valid provided that the chosen time step,  $\Delta t$ , is smaller than the mean collision time ( $t_{mct}$ ), i.e.  $\Delta t < t_{mct}$ . This operator splitting often leads to a time step error which is reduced here by utilising the Strang's splitting method to achieve second-order convergence with no intrinsic time step error.

The effect of the global body force is to accelerate the particles in the domain thereby causing the local distribution function to deviate from the global equilibrium necessitating the generation of deviational particles. The advection process displaces every particle according to the Newton's law, and interactions between particles and surfaces follow the Maxwellian reflection model where the particles interacting with the surface can be subject to a diffuse reflection with a probability of the momentum accommodation coefficient ( $\alpha=1$ ). In addition to providing an approximation of a porous media surface, the diffuse surfaces also function as a way of keeping the particle number tractable by deleting oppositely signed particles interacting with the same surface within the time step. The implementation at domain boundaries is either symmetry (specular) or periodic as appropriate for the specific study. The BGK collision term can be integrated over the time step  $\Delta t$  in the cell  $i \in N_{cell}$  which is selected taking the cell's local state into consideration. The integration is then carried out through a sequence of Markov creation and deletion events with appropriately chosen sub-time steps which are instrumental in the method's natural ability to adapt to a multi-scale system. Further details regarding the present implementation can be found in our previous work [44].

For the present stochastic method, the microscopic properties are used to compute the aggregate sum of the moments for each cell to obtain macroscopic variables. For a cell  $k$  containing  $N_k$  particles at a time step conducive to sampling, the aggregate sum of mass, momentum, and pressure tensor are given by,

$$(Agg \Sigma_m)_k = (Agg \Sigma_m)_k + \sum_{i \in N_k} s_i, \quad (7)$$

$$(Agg \Sigma_v)_k = (Agg \Sigma_v)_k + \sum_{i \in N_k} s_i \mathbf{c}_i, \quad (8)$$

$$(Agg \Sigma_p)_k = (Agg \Sigma_p)_k + \sum_{i \in N_k} s_i \mathbf{c}_i \mathbf{c}_i. \quad (9)$$

## 2.2 Surface and pore activity

A unique vantage point that is afforded by the current particle method is the ability to track the number of particles that have collided with a surface element. Thus, for every collision on the surface  $k$ , the parameter  $Agg SI$  is updated as,

$$(Agg SI)_k = (Agg SI)_k + 1. \quad (10)$$

The time-averaged version of this value signifies the role of the surface in the relaxation process of the gas molecules to an equilibrium. Termed as *surface activity*, a high value indicates that the surface is significantly involved in the development of the flow characteristics while a low value indicates that the surface plays a negligible role. This surface activity can directly quantify the role Knudsen diffusion play in gas transport in ultra-tight pore

space, which is a long-standing modelling problem. When the Knudsen diffusion becomes the dominant mechanism for gas transport, gas molecules will more likely to collide with surface rather than between themselves, so the surface activity is **relatively more significant compared to the pore activity**, which can now be quantitatively measured. When the surface activity is **relatively lower than the pore activity**, the collisions between gas molecules are more important to the gas transport, i.e. the viscous effective is more important than the Knudsen diffusion.

In porous media, the size of the pore structures varies in an extremely arbitrary fashion. The effect of these variations on the flow is seen through the co-existence of multiple regions with different degrees of rarefaction. As explored earlier, inter-molecular collisions are less likely in a region of high rarefaction whereas they are more abundant in less-rarefied regions. This effect is captured in the present particle method through the parameter termed as *pore activity* which is updated for every cell  $i \in N_{cell}$  as shown in Eq. (11) when a collision event occurs, i.e.

$$(Agg PA)_i = (Agg PA)_i + 1. \quad (11)$$

Here, the time-averaged value of the pore activity is indicative of the degree of local rarefaction at each cell. This pore activity plays a similar role as the local Knudsen number. However, it is difficult to define local Kn as the characteristic length scale can be arbitrary, while it is easy to directly measure pore activity for the present particle method. This also resolves another challenging problem for modelling flow properties of pore media when the rarefaction is important.

The hydrodynamic properties such as the number density, bulk velocity, and the pressure tensor can be obtained by summing Eqs. (7, 8, 9). The flow characteristics of complex porous media are quantified through the pore activity (Eq. (11)) and the surface activity (Eq. (10)) which are normalised by the maximum value of the pore activity  $Agg PA$  and surface activity  $Agg SI$  as demonstrated in Eq. (15) and Eq. (16) respectively.

$$\rho_j = \rho_0 + \frac{nW_{eff}}{\Delta V_j} (Agg \Sigma_m)_j, \quad (12)$$

$$\rho_j \mathbf{u}_j = \rho_0 \mathbf{u}_0 + \frac{nW_{eff}}{\Delta V_j} (Agg \Sigma_v)_j, \quad (13)$$

$$\mathbf{P}_j + \rho_j \mathbf{u}_j \mathbf{u}_j = \mathbf{P}_0 + \rho_0 \mathbf{u}_0 \mathbf{u}_0 + \frac{nW_{eff}}{\Delta V_j} (Agg \Sigma_p)_j, \quad (14)$$

$$(PA)_j = \frac{(Agg PA)_j}{(Agg PA)_{max}}, \quad (15)$$

$$(SI)_k = \frac{(Agg SI)_k}{(Agg SI)_{max}}. \quad (16)$$

### 2.3 Concepts of porous media

The flow through porous media is dependent on microscopic features such as its pore structure, connectivity, and surface area. The porosity,  $\phi$ , is defined as the volume of pore space to the total volume of a porous media sample, i.e.  $\phi = \frac{V_f}{V_t}$  and  $0 < \phi < 1$ , where  $V_f$  is the volume of the pore space,  $V_t$  is the total or bulk volume. The presence of isolated pore spaces has led to the definition of effective porosity or apparent porosity,  $\phi_{eff}$ , defined as the ratio

of the volume of pore space participating in the flow to the bulk volume, i.e.  $\phi_{eff} = \frac{V_f^{eff}}{V_t}$  and  $0 < \phi_{eff} \leq \phi$ , where  $V_f^{eff}$  is the volume of the pore space accessible to a flow.

The transport of the fluid through the porous media is described by permeability ( $\kappa$ ) [46]. Recognizing the role of fluid viscosity [47] and the potentially anisotropic, 2<sup>nd</sup>-order tensor nature of  $\kappa$  [48,49] can be expressed as

$$Q_i \propto \frac{A_{jk}\Delta P}{\mu L_i} = \kappa \frac{A_{jk}\Delta P}{\mu L_i}, \quad (17)$$

with,

$$\kappa = \begin{bmatrix} \kappa_{xx} & \kappa_{xy} & \kappa_{xz} \\ \kappa_{yx} & \kappa_{yy} & \kappa_{yz} \\ \kappa_{zx} & \kappa_{zy} & \kappa_{zz} \end{bmatrix}, \quad (18)$$

where,  $\kappa_{ij} = \mu q_i \left[ \frac{\partial P}{\partial x_j} \right]^{-1}$  and  $q_i = \frac{Q_i}{A_{jk}}$  is the volume flux,  $Q_i$  is the volume flow rate,  $A_{jk}$  is the cross sectional area of flow,  $\frac{\partial P}{\partial x_j}$  is the pressure gradient, and  $i, j, k$  are the  $x, y, z$  directions respectively.

One of the most popular corrections to the Darcy law for rarefied gases is the Klinkenberg equation [50] where the gas permeability ( $\kappa_g$ ) (often referred to as apparent permeability ( $\kappa_a$ )) is greater than the liquid permeability ( $\kappa_l$  or intrinsic permeability ( $\kappa_i$  or  $\kappa_0$ )) by a factor as shown below,

$$\kappa_g \text{ (or } \kappa_a) = \kappa_l \text{ (or } \kappa_i) \left( 1 + \frac{b}{p} \right), \quad (19)$$

where, the parameter  $b$  is termed as the Klinkenberg constant, which is indicative of the gas slippage effect. The Klinkenberg correction is usually applied to predict the initial onset of slip flow. At higher degrees of rarefaction the apparent permeability varies with  $Kn$  [51] and the second-order apparent permeability correlations have been proposed [52] as shown below,

$$\kappa_a = \kappa_i (a + bKn + cKn^2), \quad (20)$$

where,  $a, b$ , and  $c$  are correlation coefficients.

Appropriate selection of the coefficient can produce the BKC model which was put forth by Civan [53] as an improvement of the empirical scaling laws proposed by Beskok and Karniadakis [54], where  $C_r$  is the rarefaction coefficient and  $\alpha_{BKC}$  is an empirical coefficient

$$\frac{\kappa_a}{\kappa_i} = C_r \left( 1 + \frac{4Kn}{1 + Kn} \right); \quad (21)$$

$$C_r = 1 + \alpha_{BKC}Kn, \quad (22)$$

$$\alpha_{BKC} = \frac{1.358}{1 + 0.178Kn^{-0.4348}},$$

where  $\alpha_{BKC}$  is assumed to have values that are used in previous literature [55]. However, these models are extended from the results based on straight channels/pipes which are very different from complex flow geometries found in porous media. The arbitrary choice of the many empirical parameters makes these model impractical and even useless in quantifying flow properties of porous media.

The final parameter of interest in porous media flows which plays an important role in correlating porosity and permeability is tortuosity,  $\tau$ . It is by far one of the most difficult and ambiguous flow properties of porous media [56,57]. Because of rapid increase in the

computational power, calculation of tortuosity shifts away from the geometric methods [58] to those linked to the flow field [59–64]. Therefore, the tortuosity is often calculated by

$$\tau_i = \frac{\Sigma u_{mag}}{\Sigma u_i} = \frac{\langle u_{mag} \rangle}{\langle u_x \rangle}, \quad (23)$$

where,  $u_{mag}$  is the speed of the flow and  $u_i$  is the velocity in the  $i^{th}$  direction.

To understand flow properties in porous media when rarefaction is present, pore-scale studies are urgently required as the current models are based on empirical observations with arbitrary parameters.

## 2.4 Non-dimensional formulation

The non-dimensional parameters in the present work are represented by a caret (^) or are marked with a subscript  $_{ND}$  denoting non-dimensional, which are given below,

$$\begin{aligned} x_{ND} = \hat{x} &= \frac{x}{L_0}; & y_{ND} = \hat{y} &= \frac{y}{L_0}; & z_{ND} = \hat{z} &= \frac{z}{L_0}; \\ u_{ND} = \hat{u} &= \frac{u}{\varepsilon v_{mp,0}}; & v_{ND} = \hat{v} &= \frac{v}{\varepsilon v_{mp,0}}; & w_{ND} = \hat{w} &= \frac{w}{\varepsilon v_{mp,0}}; \\ n_{ND} = \hat{n} &= \frac{n}{n_0}; & T_{ND} = \hat{T} &= \frac{T}{T_0}; & P_{ND} = \hat{P} &= \frac{P}{P_0}; \\ t_{ND} = \hat{t} &= \frac{L_0 t}{v_{mp,0}}; & f_{ND} = \hat{f} &= \frac{v_{mp,0}^3}{n_0} f, \end{aligned} \quad (24)$$

where,  $L_0$  is the characteristic length of the flow domain,  $v_{mp,0}$  is the most probable speed of the molecules,  $n_0$ ,  $T_0$  and  $P_0$  are the number density, temperature and pressure of the reference state respectively. Additionally, the low-signal nature of the problem often leads to extremely small values of pressure gradients and velocity, making it necessary to scale them up to avoid computational errors. This is achieved by using  $\varepsilon$  which can be chosen such that it normalizes the largest source of non-equilibrium which is the pressure gradient in the present work and thus,

$$\hat{\zeta}_P = \frac{1}{\varepsilon} \frac{L_0}{P_0} \frac{dP}{dr_i} = 1. \quad (25)$$

Moreover, the degree of rarefaction in a flow field is often represented by the scaled rarefaction parameter as,

$$\delta_{scaled} = \frac{2}{\sqrt{\pi}} \frac{1}{Kn}. \quad (26)$$

The contour plot of a hydrodynamic property for multiple Knudsen numbers are often presented together. This juxtaposition is more amenable to comprehension if each of the cases is normalized with respect to its local maximum value. For example, we represent the velocity magnitude  $|V|$  by the local maximum normalized scaled speed ( $V_{max}$ ) defined as,

$$V_{max} = \frac{|V|}{|V|_{Max}}; V = \sqrt{u_{ND}^2 + v_{ND}^2 + w_{ND}^2}. \quad (27)$$

Among the porous media quantities, the porosity and tortuosity are dimensionless by definition. The permeability is non-dimensionalized and determined as shown below [55]

$$\kappa = 2G_p Kn, \quad (28)$$

where,

$$G_p = 2\dot{m}_{ND} = 2 \int \int n_{ND} u_{ND} dA_{ND}. \quad (29)$$

In all these studies, the reference state variables  $(n_0, T_0, P_0)$  are selected to correspond to the global equilibrium state. Here, the momentum accommodation coefficient is maintained at unity. Each structure is subjected to independent studies wherein the direction of the small non-dimensional scaled pressure gradient,  $\hat{\zeta}_p$ , is set to be in the  $X$ ,  $Y$  or  $Z$  direction. The characteristic length is taken to be the length of the unit cell that is perpendicular to the flow. The nature of the unit cells for the 3D reconstructed media results in  $L_0 = L_x = L_y = L_z$  respectively. However, for the Berea sandstone,  $L_0 = L_y$  when the pressure gradient is along the  $X$  direction and  $L_0 = L_x$  when the pressure gradient is in the  $Y$  direction. These parameters are used to normalise the problem appropriately.

### 3 Porous media

Advances in digital imaging [65] have encouraged pore-scale direct simulation of flows through geological rock samples that are digitally reconstructed from these images [66]. The main aim of the present study is to provide more in-depth insights into rarefaction effect and gas/surface interaction in gaseous flows through porous media using the LVDSMC solver we have developed, which has been extensively validated for various simple flows [44].

In all the following simulations, the image resolution has been deemed sufficient for the spatial discretization. The use of a non-uniform or refined grid [29,30,67] may improve the simulation accuracy but will challenge the assumption of a global equilibrium for all the cells. In such cases, each cell will have its own local equilibrium and the treatment of such a system leads to computational complication and stability issues due to an unrestrained increase in the number of particles [68].

#### 3.1 2D problem statement

The Berea sandstone is commonly-used in porous media studies owing to its special properties such as composition, commercial relevance and the well-sorted, well-rounded nature of its grains [69]. The current image, see Fig. 1, is engineered from a 3D Berea sandstone sample of dimensions  $1418 \times 1774 \mu m$  with an etch depth of  $24.54 \mu m$  at the Schlumberger Cambridge Research Ltd., and is of a resolution of  $453 \times 457 \times 1 \mu m$  with a porosity of approximately 30% [70]. The sample provides a wide range of pore space size and orientation in addition to a well-connected pore network.

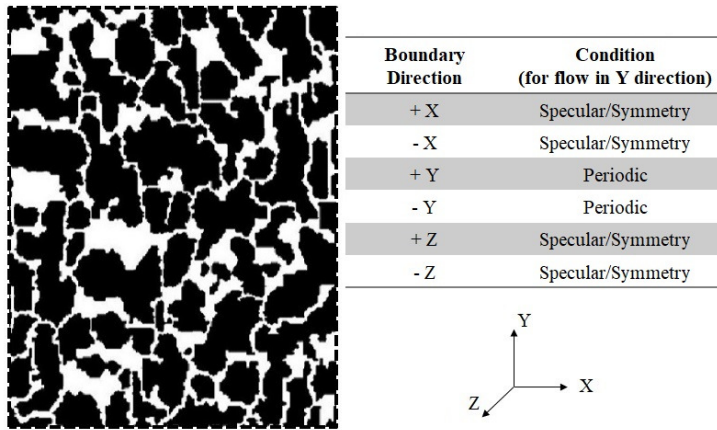


Fig. 1: Schematic of 2D image-based reconstruction of a Berea sandstone porous media (white/grey: pore space; black: solid phase).

Furthermore, the image resolution (i.e.  $453 \times 457 \times 1$ ) is kept unaltered as it is sufficiently high to be used for spatial discretization. The variation in the pore configuration is brought about by considering the pressure gradients (which corresponds to a pressure difference of 1%) in the  $X$  and  $Y$  directions independently. The effect of gaseous rarefaction is realized through the variation of the global Knudsen number defined with respect to the reference length of the sample.

### 3.2 Results and discussions: 2D porous media

The variation of flow pattern with flow direction and rarefaction demonstrates that the flow is preferential, with some flow pathways being more conducive than others leading to a greater flow speed in certain pore spaces (marked by  $(i)$  in Fig. 2). The effect of rarefaction is manifested as the gaseous slippage at the surfaces: a higher Knudsen number corresponds to larger slip at the surfaces and vice versa. This results in the narrower pore spaces (marked by  $(ii)$  in Fig. 2) being relatively inactive at  $Kn = 0.01$  in comparison to the flow at  $Kn = 10.0$ .

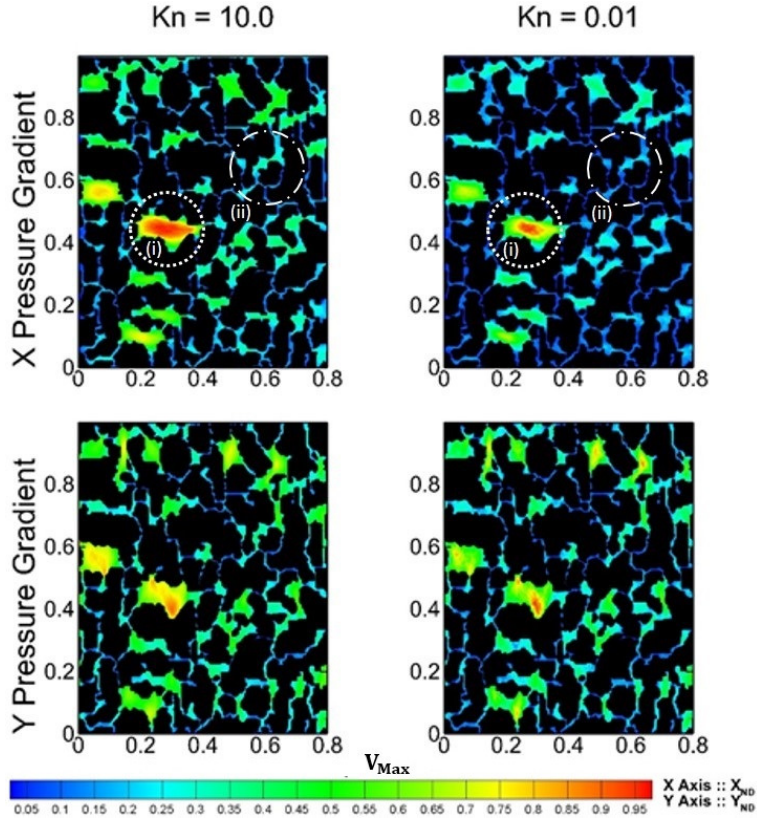


Fig. 2:  $V_{max}$  contours for 2D reconstructed porous media (Berea sandstone).

The interstitial flow patterns dictate the macroscopic properties such as the permeability and tortuosity which are plotted in Figs.3a and 3b respectively. Fig.3a shows that the permeability is higher in the  $Y$  direction than the  $X$  direction. The effect can be attributed to the tortuosity (calculated with Eq. (23)). Fig.3b indicates that the flow pathways are more tortuous in the  $X$  directional transverse flows than in the  $Y$  direction. The DVM results for the permeability in the  $y$  direction as reported by Ho *et. al.* [55] are compared with  $\kappa_{yy}$  in addition to the Klinkenberg and BKC models as shown in Fig. 4. The present results are seen to be in good agreement with the accurate DVM results.

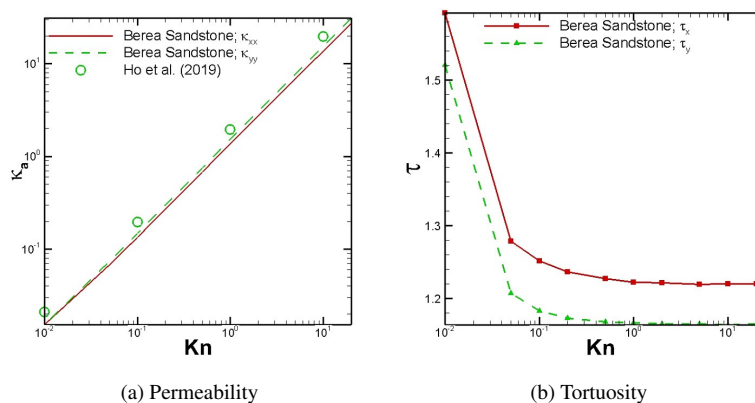


Fig. 3: The simulation results for the 2D image-based reconstructed porous media. The permeability is in the y direction as reported in Ho et al. [55].

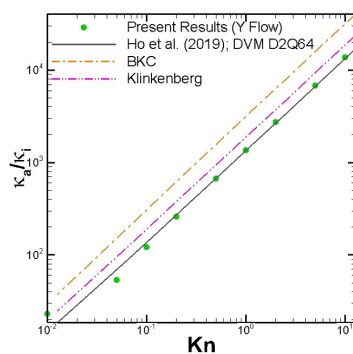


Fig. 4: Comparison of the permeability in the Y direction with the results reported in Ho et al. [55].

### 3.3 3D problem statement

The advances in imaging technology have enabled pore-scale simulations using digital images of real samples. Here, we will use 5 reconstructed 3D samples in the following study, which are the synthetic packs, including a Bead Pack (BP) made up of glass spheres of  $1.59 \mu m$  diameter and the voxel side length of  $17.472 \mu m$  [71], and a LRC32 grade fluvial Sand Pack (SP) of the voxel side length of  $9.184 \mu m$  [71], and the geological samples of natural rocks, including a Castlegate (CG) sandstone sample, a fossiliferous Gambier (GB) sandstone sample, and a clastic sedimentary Fayetteville Shale (SH) sample with the voxel lengths of  $5.6 \mu m$  [71],  $3.024 \mu m$  [71], and  $4.6 \mu m$  [72] respectively. The depiction of these samples are presented in Fig. 5 with the respective voxel resolution specified in brackets.

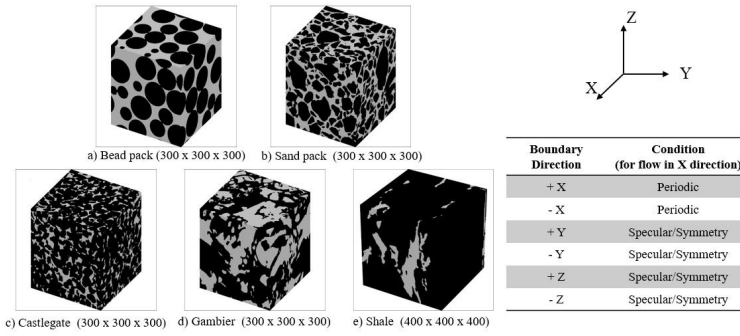


Fig. 5: 3D image-based reconstruction of the synthetic packs and the rock samples (white/grey: pore space; black: solid phase)

Each of these samples is subjected to a wide range of rarefied flows, with an applied small pressure gradient (which corresponds to a pressure difference of 1%) in the  $X$ ,  $Y$ , or  $Z$  direction. The Maxwellian diffuse surfaces are assumed with the accommodation coefficient  $\alpha = 1.00$ .

### 3.4 Results and discussions: 3D porous media

The flow driven by a pressure gradient in the  $X$  direction at  $Kn = 1.00$  is depicted for these 5 samples in Fig. 6. Unlike their 2D counterparts, the contours (Fig. 6) for a 3D reconstructed porous media only provide a general overview of the flow fields due to their complicated internal structure. The primary characterization has traditionally been the normalized permeability as presented in Figs. 7 and 8. The normalization is performed using the intrinsic permeability which is obtained from the LBM simulation utilizing a  $D3Q19$  model with the non-slip bounce-back reflection on the surfaces. The results obtained are compared against the Klinkenberg and BKC models for all the considered rock samples. Additionally, the results are compared with the DVM results using different resolutions in the velocity space as reported by Ho *et. al.* [55] for the sand pack (Fig. 7a) and the shale rock (Fig. 7b) samples. The DVM results are seen to follow the trend predicted by the models while the present results agree well with the accurate DVM results with a higher resolution in the velocity space. **Note: the LBM model is well-suited for continuum flows to provide efficient prediction of intrinsic permeability but is not expected to capture rarefaction effect in a non-equilibrium flow.**

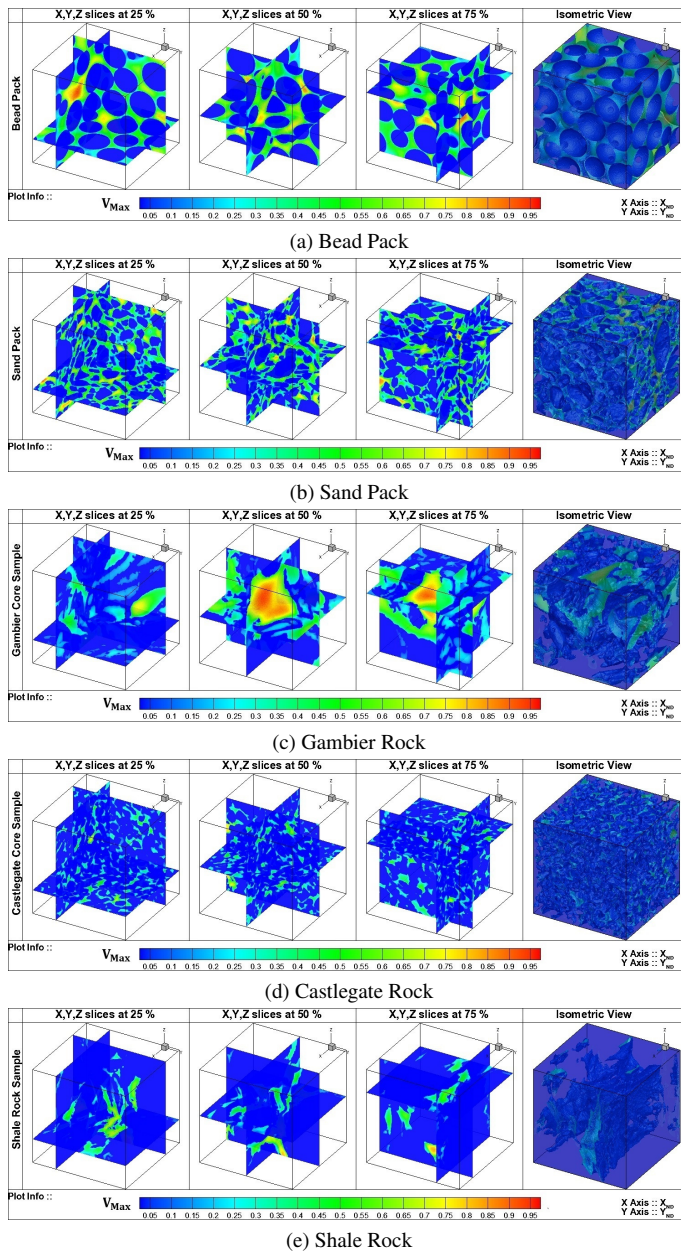


Fig. 6:  $V_{max}$  contours for 3D reconstructed porous media.

The permeabilities predicted by the present method for the additional samples such as the bead pack, Castlegate and Gambier (Fig. 8) are also compared to the results of the Klinkenberg and BKC models. The results exhibit a better agreement with the a higher-order permeability model indicating that effect of the complex flow pathways and multi-scale nature cannot be predicted by a linear permeability model [73]. **However, high-order models such as the BKC model involve more unknown parameters which may be tuned to obtain better results but are not practically useful to make accurate predictions.** It is to be noted that as a special form of DSMC, the present method is not designed for the continuum flow where  $Kn$  is close to zero which explains the discrepancy in the results for  $Kn = 0.01$ . **There are recent rapid development of multiscale kinetic schemes, which may be considered for efficient pore-scale simulations covering flowfield from continuum to free molecular.** For example, the unified gas kinetic schemes [74], the discrete unified gas kinetic scheme [75, 76], and the general synthetic iterative scheme [77,78] are among these computationally efficient deterministic schemes.

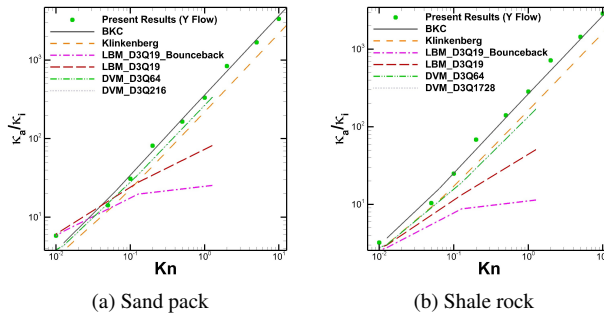


Fig. 7: The permeability for the 3D image-based reconstructed porous media in the Y direction compared to the reported results [55]: (a) sand pack; (b) shale rock.

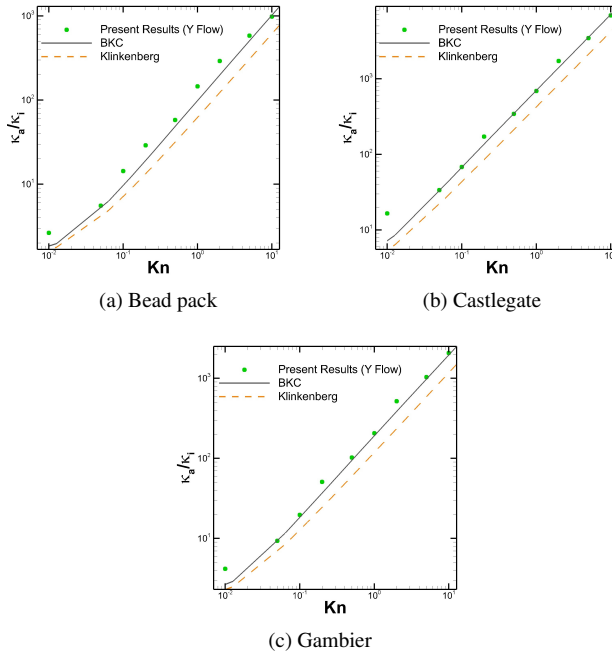


Fig. 8: The permeability for the 3D image-based reconstructed porous media in the Y direction.

The anisotropic nature of the permeability matrix, calculated by Eq. (18) is shown below

$$\begin{aligned}
 & \begin{bmatrix} K_{xx} & K_{xy} & K_{xz} \\ K_{yx} & K_{yy} & K_{yz} \\ K_{zx} & K_{zy} & K_{zz} \end{bmatrix} \\
 &= \left\{ \begin{array}{l} \begin{bmatrix} 3.4876 & 0.0395 & 0.0348 \\ 0.0398 & 3.6464 & 0.0065 \\ 0.0346 & 0.0066 & 3.3412 \end{bmatrix} \\ \xrightarrow[\%]{\text{Max. Normalized}} \\ \begin{bmatrix} 95.65 & 1.08 & 0.95 \\ 1.09 & 100.00 & 0.18 \\ 0.95 & 0.18 & 91.63 \end{bmatrix} \end{array} \right\} \text{Bead Pack} \\
 &= \left\{ \begin{array}{l} \begin{bmatrix} 1.6214 & 0.0097 & 0.0127 \\ 0.0096 & 1.6350 & 0.0167 \\ 0.0126 & 0.0167 & 1.4859 \end{bmatrix} \\ \xrightarrow[\%]{\text{Max. Normalized}} \\ \begin{bmatrix} 99.17 & 0.59 & 0.78 \\ 0.59 & 100.00 & 1.02 \\ 0.77 & 1.02 & 90.88 \end{bmatrix} \end{array} \right\} \text{Sand Pack} \\
 &= \left\{ \begin{array}{l} \begin{bmatrix} 0.5430 & 0.0011 & 0.0027 \\ 0.0011 & 0.4915 & 0.0031 \\ 0.0027 & 0.0031 & 0.5132 \end{bmatrix} \\ \xrightarrow[\%]{\text{Max. Normalized}} \\ \begin{bmatrix} 100.00 & 0.20 & 0.49 \\ 0.20 & 90.50 & 0.57 \\ 0.50 & 0.58 & 94.51 \end{bmatrix} \end{array} \right\} \text{Castlegate Rock} \\
 &= \left\{ \begin{array}{l} \begin{bmatrix} 4.6390 & 0.0049 & 0.0849 \\ 0.0050 & 4.0274 & 0.1401 \\ 0.0846 & 0.1403 & 4.1871 \end{bmatrix} \\ \xrightarrow[\%]{\text{Max. Normalized}} \\ \begin{bmatrix} 100.00 & 0.10 & 1.83 \\ 0.11 & 86.82 & 3.02 \\ 1.82 & 3.02 & 90.26 \end{bmatrix} \end{array} \right\} \text{Gambier Rock} \\
 &= \left\{ \begin{array}{l} \begin{bmatrix} 1.4427 & 0.0259 & 0.0115 \\ 0.0258 & 1.1414 & 0.0177 \\ 0.0116 & 0.0177 & 1.4315 \end{bmatrix} \\ \xrightarrow[\%]{\text{Max. Normalized}} \\ \begin{bmatrix} 100.00 & 1.79 & 0.80 \\ 1.79 & 79.11 & 1.23 \\ 0.80 & 1.23 & 99.22 \end{bmatrix} \end{array} \right\} \text{Shale Rock}
 \end{aligned} \tag{30}$$

The above matrix is seen to be diagonal dominant, suggesting that the flow is principally in the direction of the small pressure gradient. Furthermore, the maximum diagonal element in each sample indicates the most permeable direction for that sample. Accordingly, it is seen to be the  $Y$  directional flow (since  $\kappa_{yy}$  is dominant) is preferred for the synthetic packs (BP and SP) whereas, the  $X$  directional flow is preferred among the rock samples (CG, BP, and SH) as indicated by the dominance of  $\kappa_{xx}$ .

The numerical interpretation of the permeability can be obtained by the dimensional value as  $\kappa_a \varepsilon L_0^2$  where,  $L_0$  is considered as the side on the cubic voxel, and is thus different for each of the 3D reconstructed media. For the  $X$  directional flow through the shale rock sample at  $Kn = 1.00$ , the non-dimensional permeability,  $\kappa_a = 1.4427$ , translates to a dimensional permeability of  $1.4427 \times 10^{-3} \times (4.6 \times 10^{-6})^2 m^2 = 30.52 md$  ( $md$ : milidarcys) which is in close agreement with the value of  $29.30 md$  predicted for the same shale rock sample under similar rarefaction conditions reported by Ho *et. al.* [55].

### 3.5 Results and discussions: pore and surface activity

The pore activity is calculated at a cellular level and a high pore activity is synonymous with a high number of inter-molecular collisions in a time interval which is a feature of a low- $Kn$  flow. In order for a cell to possess a high pore activity, it must be inside a pore space (collection of connected cells) that is large enough to sustain a low degree of local rarefaction, in addition to being far away from surface. If a sample contains a large population of cells with high pore activity, then the sample either contains numerous large pores or a few very large pores. The large flow area coupled with the low degree of local rarefaction provides an environment which is conducive to transport via viscous diffusion as opposed to Knudsen diffusion. The above explanation is illustrated in Fig. 9 for an example of low and high activity cells and the corresponding pore spaces.

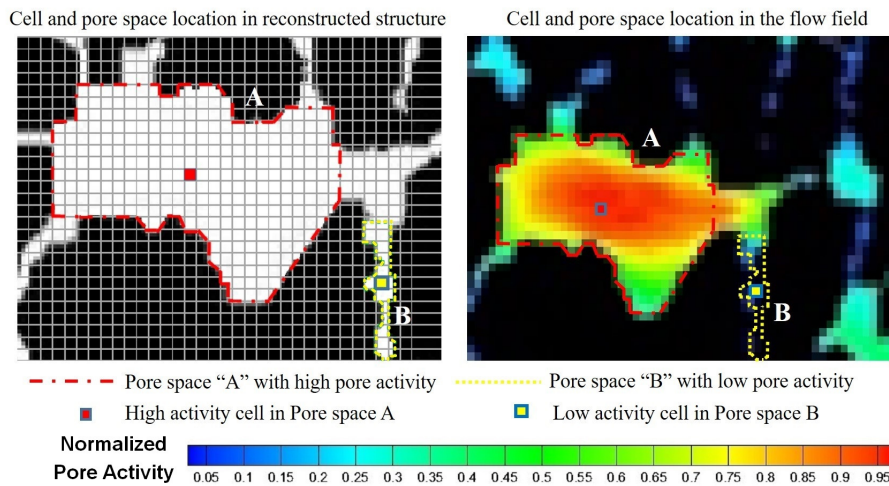


Fig. 9: Illustration of the concept of pore activity in the cell and pore space.

In all these 3D samples, the population of pores exhibiting a non-zero activity is essentially the same as the sample porosities because the isolated pores do not contribute to mass flow. The porosity computed by considering active pore population is compared to the reported porosity of the samples in Tab. 1 where an excellent agreement is observed. The small discrepancy is due to inaccuracies in re-construction of flow geometries using the digital images. Therefore, the pore activity provides a new way of evaluating effective porosity.

Table 1: Porosity determination using pore activity compared to the reported values.

Sample	Porosity (reported)	Porosity (computed)
Berea Sandstone	0.32 [71]	0.321
Bead Pack	0.379 [71]	0.371
Sand Pack	0.363 [71]	0.377
Castlegate	0.206 [71]	0.224
Gambier	0.436 [71]	0.438
Shale	0.170 [72]	0.172

The surface activity can be best understood as a classification of the role of surface in gas transport. For low activity, the surface must have a small number of particles reflecting off it, which leads to small flow resistance, while a surface with high activity would have a large number of particles colliding with it.

A clearer demonstration of the surface activity is presented by plotting the value on the various surface elements of the 2D Berea sandstone sample, which we call surface activity distribution, as presented in fig. 10. The flow from left to right due to a X-directional pressure gradient and the flow from bottom to top caused by a Y-directional pressure gradient at  $Kn = 1.00$  are considered. The permeability for these cases has been reported previously in fig. 3a.

The surface activity distributions presented in fig. 10 show that, as expected, the same surface elements have different surface behaviour in each case. For brevity and clarity, we examine the ‘Region A’ and the ‘Region B’ in detail which are marked in fig. 10a and separately highlighted in figs. 10b and 10c respectively. In Region A, we isolate our consideration to two void spaces labelled (i) and (ii), which were previously demarcated in fig. 9 as the pore space ‘A’ and ‘B’ respectively. Void (i) and (ii) are important pathways in the X and Y directional flows respectively, and the relative sizes dictate that the viscous transport dominates the void (i) whereas, the Knudsen diffusion dominates the void (ii). This is further reinforced by fig. 10b which indicates that, in the X directional flow, the surfaces of the void (i) are only slightly more active than the void (ii) despite the void (i) being a critical region in the flow pathway. On the contrary, in the Y-directional flow, the contribution of the void (ii) is more important and the domination of Knudsen diffusion is evident from the very high activity of its surfaces.

The attention in Region B is isolated to the grain that is completely surrounded by gas during the flow. The top surface of the grain is denoted as (i) while the bottom surface is labelled as (ii). In the Y-directional flow, the bottom surface (ii) has larger surface activities since gas molecules collide more frequently there than the top surface (i) owing to the orientation of the flow (from bottom to top). Meanwhile, the top surface (i) is more active in the X-directional flow since the path of least resistance for this flow passes above the grain and there is no incentive for the flow to interact with the bottom surface, i.e. the surface (ii) of the grain.

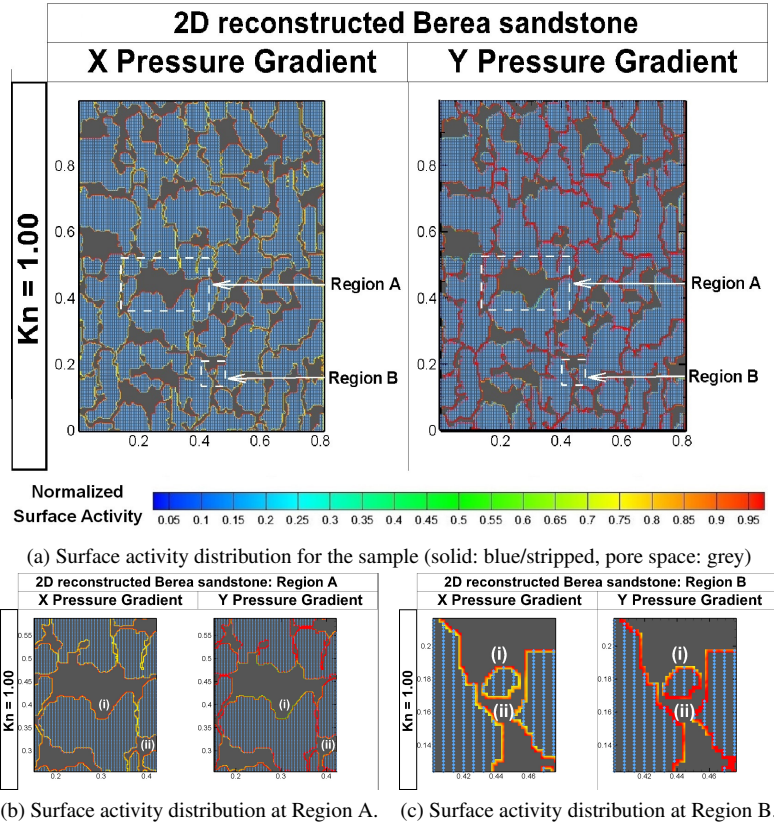


Fig. 10: Illustration of the concept of surface activity for the Berea sandstone.

Together with the pore activity, we can clearly characterize the underlying gas transport mechanisms in different regions. When the flow is dominated by viscous force, the pore activity must be high (as is the case in the pore space A in fig. 9) in comparison with the surface activity (as is the case in the void (i) of Region A in fig. 10b). When the surface activity increases (as is the case in the void (ii) of Region A in fig. 10b), Knudsen diffusion becomes more important and the pore activity becomes negligible indicating poor transport by viscous force (as is the case in the pore space B in fig. 9). A more detailed measurement of two activities for consistent comparison and meaningful extension to 3D flows will be required, which will be our future research.

#### 4 Computational performance analysis

All computations were performed on a workstation comprising of dual Intel(R) Xeon(R) CPU E5 – 2630 v3 @ 2.40GHz x86 – 64 architecture and implementation of the parallel framework is done through domain decomposition although the domain considered is the pore space. Appropriate load balancing is ensured by allocating an equal size (approximately) of pore space per MPI processor.

In a given time step, the collision process is the most computationally expensive operation for low- $Kn$  flows, which is highlighted for the Gambier and Castlegate outcrops in Figs. 11a and 11b respectively, where the time taken by the individual processes are broken down and presented. The processes of indexing, convergence verification, sampling and other housekeeping operations are classified under the miscellaneous (Misc.) piece of the pie. It is evident that as the rarefaction decreases (inner to outer ring) the computational time consumed by the collision processes increases. This effect manifests itself as an increased computational time at lower degrees of rarefactions as noted.

For instance, for the  $Kn = 0.001$  flows, it takes an extremely long time to achieve steady state and hence the results are not presented. The domination of collisions in this regime requires the generation and deletion of a large number of particles in addition to a regeneration of these particles to rectify the assigned sign and ensure mass conservation during every time step. While this is an anticipated pitfall as the LVDSMC method was never designed for such continuum flows, it limits the method's ability to reconcile porous media structures where rarefied regions co-exist with, an otherwise predominantly, continuum flow.

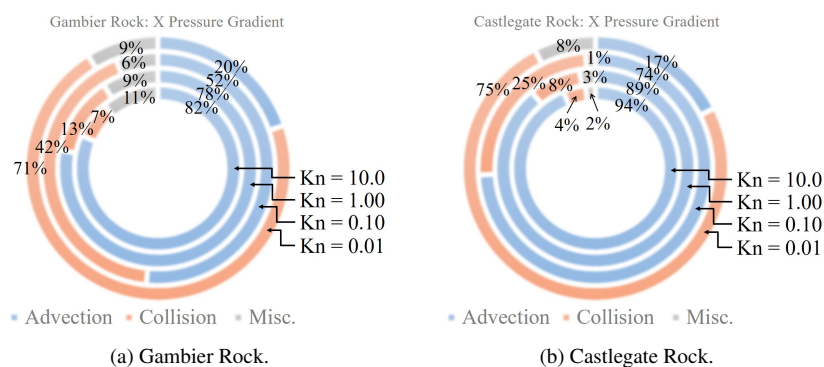


Fig. 11: Computational time breakup for the individual process involved.

The computational performance of the current particle method is critically dependent on a number of parameters such as cell size, time step, number of ensembles and the particles used per cell. At present, the time step is enforced to be less than the mean collision time, and the cell size, usually restricted to a fraction of the mean free path, is maintained equal to the resolution of the image as this is found to be convenient. The main sources contributing to the uncertainty are the number of particles per cell (PPC) and the number of ensembles. The number of ensembles for the 3D porous media structures is set to 10, which is observed to be sufficient for a reliable average. **Each ensemble is an independent run where each run consists of the generation and sampling of 100,000 samples after the steady state is attained. 10 ensembles have shown to yield the best mean value for the lowest  $Kn (=0.01)$  considered here, so it is safely used for all the other larger  $Kn$  cases.** To ascertain the effect of PPC on the current implementation, the permeability for the image-reconstructed porous media is revisited with degree of uncertainty characterized by the standard deviation. **As a large number of particles are used for PPC of 100, a single ensemble seems to be sufficient. Additionally, the core idea of this study is to determine the effect of using lower numbers**

of PPC, thus, the focus is on PPC = 20 and PPC = 5. The results for all the reconstructed images is provided in Tab. 2 for  $Kn = 1.00$ .

Table 2: The standard deviation in permeability of the reconstructed media due to the pressure gradients in the X, Y, and Z directions at  $Kn = 1.00$  for various PPC and 10 ensembles.

Kn = 1.00		PPC = 100	PPC = 20		PPC = 5	
	Direction		Mean	$\sigma$	Mean	$\sigma$
Bead Pack	X	3.4877	3.4876	1.69E-06	3.2765	3.02E-02
	Y	3.6461	3.6464	4.38E-05	3.3950	4.17E-02
	Z	3.3411	3.3412	9.87E-06	3.1312	3.42E-02
Sand Pack	X	1.6213	1.6214	7.95E-06	1.4920	2.29E-02
	Y	1.6351	1.6350	1.14E-05	1.4752	2.53E-02
	Z	1.4859	1.4859	1.53E-06	1.3819	1.75E-02
Gambier	X	0.5430	0.5430	9.19E-07	0.4971	7.08E-03
	Y	0.4914	0.4915	4.28E-06	0.4715	3.19E-03
	Z	0.5132	0.5132	4.48E-07	0.5012	1.98E-03
Castlegate	X	4.6390	4.6390	4.55E-06	4.1799	6.80E-02
	Y	4.0275	4.0274	4.37E-06	4.0074	3.19E-03
	Z	4.1871	4.1871	1.88E-06	4.0571	2.42E-02
Shale	X	1.4427	1.4427	3.97E-06	1.3627	1.51E-02
	Y	1.1413	1.1414	1.38E-05	1.1404	1.64E-04
	Z	1.4313	1.4313	2.06E-08	1.4301	1.99E-04

Table 3: The standard deviation in permeability of the reconstructed media due to the pressure gradients in the X, Y, and Z directions at  $Kn = 0.01$  for various PPC and 10 ensembles.

Kn = 0.01		PPC = 100	PPC = 20		PPC = 5	
	Direction		Mean	$\sigma$	Mean	$\sigma$
Bead Pack	X	0.0670	0.0671	3.20E-05	0.0430	8.95E-02
	Y	0.0661	0.0662	3.23E-05	0.0591	6.21E-02
	Z	0.0632	0.0630	6.36E-05	0.0520	7.54E-02
Sand Pack	X	0.0290	0.0292	7.78E-05	0.0221	2.19E-02
	Y	0.0286	0.0288	7.21E-05	0.0203	6.19E-02
	Z	0.0378	0.0371	2.94E-04	0.0326	6.66E-03
Castlegate	X	0.0136	0.0136	6.62E-06	0.0186	5.80E-03
	Y	0.0118	0.0118	1.30E-05	0.0180	9.48E-02
	Z	0.0116	0.0117	1.41E-05	0.0161	4.11E-02
Gambier	X	0.1110	0.1118	2.19E-04	0.1197	7.56E-02
	Y	0.0813	0.0814	1.12E-05	0.0850	4.32E-02
	Z	0.1168	0.1168	5.53E-06	0.1835	8.69E-02
Shale	X	0.0340	0.0345	1.63E-04	0.0300	6.49E-02
	Y	0.0129	0.0129	5.25E-06	0.0190	9.23E-02
	Z	0.0337	0.0337	1.99E-06	0.0371	8.54E-02

The PPC is a parameter that determines the weight of a particle and as such a reasonable estimate of the PPC (i.e. 20) is sufficient. While an extremely low value (PPC = 5) is undesirable due to the increased uncertainty of the result, a very high value (PPC = 100) will increase the associated computational time in exchange for a small reduction in the degree of uncertainty. Additionally, a very low PPC will lead to high particle weights and could result in non-physical results such as a negative density and temperature.

## 5 Conclusions

The LVDSMC solver is developed to enable pore-scale multiscale simulations to provide new insights gas transport in ultra-tight porous media. The effects of rarefaction and surface/gas interactions are captured by two new parameters, i.e. pore and surface activity respectively. The computational efficiency and accuracy as well as its limitation has been analysed, suggesting that this new solver can be useful for pore-scale study of multiscale gas flows.

The performance of the method against other similar-spirited methods, such as the DS-BGK [25, 26, 29, 30] may yield more insights and will be an interesting future research topic. Another avenue for improvement is the limitation to treating lower-Kn regions which will hamper the method's potential in porous media simulations where local regions of lower-Kn are plentiful. In such cases, the recently-developed multiscale kinetic schemes [74–79] may be considered for efficient pore-scale simulations.

**Acknowledgements** We wish to thank Dr. Minh Tuan Ho of Edinburgh University UK, Dr. Lei Wu of Southern University of Science and Technology, China, and Dr. Thomas Burel of Strathclyde University, UK for useful discussion and suggestions.

## Conflict of interest

The authors declare that they have no conflict of interest.

## References

1. B. Antohe, J. Lage, D. Price, R.M. Weber, *International Journal of Heat and Fluid Flow* **17**(6), 594 (1996)
2. G. Tang, C. Bi, Y. Zhao, W. Tao, *Energy* **90**, 701 (2015)
3. S.W. Cha, R. O'Hayre, F.B. Prinz, *Solid State Ionics* **175**(1-4), 789 (2004)
4. A.A. Merrikh, J.L. Lage, *Journal of biomechanical engineering* **127**(3), 432 (2005)
5. Y. Yang, K. Wang, L. Zhang, H. Sun, K. Zhang, J. Ma, *Fuel* **251**, 683 (2019)
6. J. Lachaud, N. Mansour, in *48th AIAA Aerospace Sciences Meeting Including the New Horizons Forum and Aerospace Exposition* (2010), p. 984
7. M. Wang, W. Zhu, *International Journal of Heat and Mass Transfer* **96**, 29 (2016)
8. P.L. Bhatnagar, E.P. Gross, M. Krook, *Phys. Rev.* **94**(3), 511 (1954)
9. E. Shakhov, *Fluid Dynamics* **3**(5), 95 (1968)
10. L.H. Holway Jr, *The physics of fluids* **9**(9), 1658 (1966)
11. Y. Zhang, R. Qin, D.R. Emerson, *Physical review E* **71**(4), 047702 (2005)
12. C. Shen, D. Tian, C. Xie, J. Fan, *Microscale Thermophysical Engineering* **8**(4), 423 (2004)
13. Y.H. Zhang, X.J. Gu, R.W. Barber, D.R. Emerson, *Physical Review E* **74**(4), 046704 (2006)
14. J. Meng, Y. Zhang, N.G. Hadjiconstantinou, G.A. Radtke, X. Shan, *Journal of Fluid Mechanics* **718**, 347 (2013)
15. T. Platkowski, R. Illner, *SIAM review* **30**(2), 213 (1988)
16. P. Wang, M.T. Ho, L. Wu, Z. Guo, Y. Zhang, *Computers & Fluids* **161**, 33 (2018)
17. L. Wu, J. Zhang, H. Liu, Y. Zhang, J.M. Reese, *Journal of Computational Physics* **338**, 431 (2017)
18. W. Yang, X.J. Gu, L. Wu, D.R. Emerson, Y. Zhang, S. Tang, *Journal of Computational Physics* p. 109397 (2020)
19. R.P. Nance, D.B. Hash, H. Hassan, *Journal of Thermophysics and Heat Transfer* **12**(3), 447 (1998)
20. C. Cai, I.D. Boyd, J. Fan, G.V. Candler, *Journal of thermophysics and heat transfer* **14**(3), 368 (2000)
21. J. Fan, C. Shen, *Journal of Computational Physics* **167**(2), 393 (2001)
22. Q. Sun, I.D. Boyd, *Journal of Computational Physics* **179**(2), 400 (2002)
23. J. Chun, D. Koch, *Physics of Fluids* **17**(10), 107107 (2005)
24. C. White, M.K. Borg, T.J. Scanlon, J.M. Reese, *Computers & Fluids* **71**, 261 (2013)
25. J. Li, in *AIP Conference Proceedings*, vol. 1333 (2011), vol. 1333, pp. 283–288

26. J. Li, in *AIP Conference Proceedings*, vol. 1501 (2012), vol. 1501, pp. 849–856
27. M.T. Ho, J. Li, L. Wu, J.M. Reese, Y. Zhang, *Computers & Fluids* **181**, 143 (2019)
28. M.T. Ho, J. Li, W. Su, L. Wu, M.K. Borg, Z. Li, Y. Zhang, *Journal of Fluid Mechanics* **901** (2020)
29. J. Li, A.S. Sultan, et al., in *International Petroleum Technology Conference* (International Petroleum Technology Conference, 2015)
30. J. Li, A.S. Sultan, *Journal of Natural Gas Science and Engineering* **48**, 197 (2017)
31. L.L. Baker, N.G. Hadjiconstantinou, *Physics of Fluids* **17**(5), 051703 (2005)
32. L.L. Baker, N.G. Hadjiconstantinou, in *ASME 4th International Conference on Nanochannels, Microchannels, and Minichannels* (American Society of Mechanical Engineers, 2006), pp. 377–383
33. T.M. Homolle, N.G. Hadjiconstantinou, *Journal of Computational Physics* **226**(2), 2341 (2007)
34. T.M. Homolle, N.G. Hadjiconstantinou, *Physics of Fluids* **19**(4), 041701 (2007)
35. N.G. Hadjiconstantinou, G.A. Radtke, L.L. Baker, arXiv preprint arXiv:0905.2218 (2009)
36. G.A. Radtke, N.G. Hadjiconstantinou, *Physical Review E* **79**(5), 056711 (2009)
37. G.A. Radtke, N.G. Hadjiconstantinou, W. Wagner, *Physics of fluids* **23**(3), 030606 (2011)
38. H.A. Al-Mohssen, N.G. Hadjiconstantinou, *ESAIM: Mathematical Modelling and Numerical Analysis* **44**(5), 1069 (2010)
39. M.T. Ho, L. Wu, I. Graur, Y. Zhang, J.M. Reese, *International Journal of Heat and Mass Transfer* **126**, 1222 (2016)
40. M.R. Allshouse, N.G. Hadjiconstantinou, in *AIP Conference Proceedings*, vol. 1084 (AIP, 2008), vol. 1084, pp. 1015–1020
41. N.G. Hadjiconstantinou, G.A. Radtke, L.L. Baker, *Journal of Heat Transfer* **132**(11), 112401 (2010)
42. G.A. Radtke, N.G. Hadjiconstantinou, S. Takata, K. Aoki, *Journal of Fluid Mechanics* **707**, 331 (2012)
43. G.A. Radtke, J.P.M. Péraud, N.G. Hadjiconstantinou, *Philosophical Transactions of the Royal Society A: Mathematical, Physical and Engineering Sciences* **371**(1982), 20120182 (2013)
44. F.D. Bosco, Y. Zhang, *Physics of Fluids* **32**(8), 082002 (2020)
45. C. Cercignani, A. Daneri, *Journal of Applied Physics* **34**(12), 3509 (1963)
46. H.P.G. Darcy, *Les Fontaines publiques de la ville de Dijon. Exposition et application des principes à suivre et des formules à employer dans les questions de distribution d'eau, etc* (V. Dalmont, 1856)
47. M. Muskat, R. Wyckoff, H. Botset, M. Meres, et al., *Transactions of the AIME* **123**(1), 69 (1937)
48. B. Ghanbarian, F. Javadpour, *Journal of Geophysical Research: Solid Earth* **122**(4), 2541 (2017)
49. R. Guibert, M. Nazarova, P. Horgue, G. Hamon, P. Creux, G. Debenest, *Transport in Porous Media* **107**(3), 641 (2015)
50. L. Klinkenberg, et al., in *Drilling and production practice* (American Petroleum Institute, 1941)
51. F. Civan, *Transport in porous media* **82**(2), 375 (2010)
52. G. Tang, W. Tao, Y. He, *Physical Review E* **72**(5), 056301 (2005)
53. F. Civan, *Transport in porous media* **82**(2), 375 (2010)
54. A. Beskok, G.E. Karniadakis, *Microscale Thermophysical Engineering* **3**(1), 43 (1999)
55. M.T. Ho, L. Zhu, L. Wu, P. Wang, Z. Guo, J. Ma, Y. Zhang, *Fuel* **249**, 341 (2019)
56. J. Bear, *Dynamics of fluids in porous media* (Elsevier, New York., 1972)
57. M.B. Clennell, *Geological Society of London* **122**(1), 299 (1997)
58. Y. Bo-Ming, L. Jian-Hua, *Chinese Physics Letters* **21**(8), 1569 (2004)
59. A. Koponen, M. Kataja, J. Timonen, *Physical Review E* **54**(1), 406 (1996)
60. A. Koponen, M. Kataja, J. Timonen, *Physical Review E* **56**(3), 3319 (1997)
61. M. Matyka, A. Khalili, Z. Koza, *Physical Review E* **78**(2), 026306 (2008)
62. M. Matyka, Z. Koza, in *AIP Conference Proceedings*, vol. 1453 (AIP, 2012), vol. 1453, pp. 17–22
63. A. Duda, Z. Koza, M. Matyka, *Physical Review E* **84**(3), 036319 (2011)
64. A. Nabovati, A. Sousa, in *New Trends in Fluid Mechanics Research* (Springer, 2007), pp. 518–521
65. D. Wildenschild, A.P. Sheppard, *Advances in Water Resources* **51**, 217 (2013)
66. M.T. Ho, L. Zhu, L. Wu, P. Wang, Z. Guo, Z.H. Li, Y. Zhang, *Computer Physics Communications* **234**, 14 (2019)
67. J. Li, *Fuel* **250**, 154 (2019)
68. T.T.M.M. Homolle, Efficient particle methods for solving the Boltzmann equation. Ph.D. thesis, Massachusetts Institute of Technology (2007)
69. P. Churcher, P. French, J. Shaw, L. Schramm, et al., in *SPE International Symposium on Oilfield Chemistry* (1991), 21044, pp. 431–446
70. E.S. Boek, M. Venturoli, *Computers & Mathematics with Applications* **59**(7), 2305 (2010)
71. A. Sheppard, M. Prodanovic. Network generation comparison forum. <http://www.digitalrocksportal.org/projects/16> (2015). DOI doi:10.17612/P7059V
72. B. Bai, M. Elgmati, H. Zhang, M. Wei, *Fuel* **105**, 645 (2013)
73. L. Wu, M.T. Ho, L. Germanou, X.J. Gu, C. Liu, K. Xu, Y. Zhang, *Journal of Fluid Mechanics* **822**, 398 (2017)

74. K. Xu, J.C. Wang, *Journal of Computational Physics* **229**, 7747 (2010)
75. Z. Guo, K. Xu, W. R, *Physical Review E* **88**(3), 033305 (2013)
76. P. Wang, M.T. Ho, L. Wu, Z. Guo, Y. Zhang, *Computers & Fluids* **161**, 33 (2018)
77. W. Su, L. Zhu, P. Wang, Y. Zhang, L. Wu, *Journal of Computational Physics* **407**, 109245 (2020)
78. L. Zhu, C. Pi, W. Su, Z. Li, Y. Zhang, L. Wu, *Journal of Computational Physics* **430**, 110091 (2021)
79. W. Su, Y. Zhang, L. Wu, *Computer Methods in Applied Mechanics and Engineering* **373**, 113548 (2021)